

LEAST-SQUARES REVERSE TIME MIGRATION OF PURE QP-WAVE IN ANISOTROPIC MEDIA USING LOW-RANK FINITE DIFFERENCE

GUOCHAO GAO¹, JINQIANG HUANG^{2*} and ZHENCHUN LI³

¹*Aix Marseille Univ, CNRS, Centrale Marseille, Institut Fresnel, Marseille 13397, France.*

²*Resource and Environmental Engineering College, Guizhou University, Guiyang 550025, China. 1194998838@qq.com*

³*School of Geosciences, China University of Petroleum (East China), Qingdao 266580, P.R. China.*

(Received December 11, 2019; revised version accepted December 20, 2020)

ABSTRACT

Gao, G.C., Huang, J.Q. and Li, Z.C., 2021. Least-squares reverse time migration of pure qp-wave in anisotropic media using low-rank finite difference. *Journal of Seismic Exploration*, 30: 121-146.

The pseudo-acoustic least-squares reverse time migration (PA-LSRTM) is often used for imaging of anisotropic media. Due to acoustic approximation, it, however, shows severe instability in the forward simulation, strong quasi-SV (qSV) wave residual in the demigration record, and terrible numerical dispersion in tilted transversely isotropic (TTI) media. The low-rank finite-difference (LFD) approach can effectively overcome these problems, but existing research only focuses on forward modeling, and no examples are found in LSRTM. For the first time in this paper, we derive the pure qP-wave linearized forward modeling and migration operators in TTI media with the help of LFD. Then, we implement pure qP-wave least-squares reverse time migration (LFD-LSRTM) in the inversion scheme. To improve the inversion efficiency, the plane-wave encoding technique is used, and to increase its robustness, the prestack parameterization is adopted. Finally, we obtain the prestack plane-wave least-squares reverse time migration (LFD-Pre-PLSRTM). Examples demonstrate that our method provides significant advantages in imaging TTI media, yielding satisfactory results with less expensive computation and more stable convergence compared to PA-LSRTM. More importantly, the proposed method can successfully avoid troubles caused by the acoustic approximation, and reasonably allow errors in the parameter model and noise in the data, making it possible to deal with real data.

KEY WORDS: anisotropy, least-squares migration, pure qP-wave, low-rank finite difference, inversion.

INTRODUCTION

Least-squares reverse time migration (LSRTM) has already become a useful imaging method in the seismic exploration due to its superiority in the spatial resolution. The conventional LSRTM is always under an isotropic assumption, so it inevitably produces the degraded image in an anisotropic medium, manifesting as increased imaging error, reduced resolution, severe migration noise, and even divergent iteration when the anisotropy is strong. Since the anisotropy is widely observed in the subsurface, many methods were developed to address it, including elliptical approximation, weak-anisotropy approximation, and acoustic approximation. The most commonly used pseudo-acoustic wave equation derived from the acoustic approximation (Alkhalifah, 1998) dramatically simplifies the anisotropic wave equation. However, the pseudo-acoustic wave equation cannot completely avoid qSV-wave, and the qSV-wave residuals always couple with the desired qP-wave when performing migration or demigration (i.e., linearized forward modeling). Another issue is computation stability, especially in the region with strong anisotropy. Therefore, LSRTM, based on the pseudo-acoustic wave equation, is still challenging. To effectively image in anisotropic media, it is critical to obtain pure qP-wave accurately and stably.

The theory of least-squares migration (LSM) was first established by Tarantola (1984) in exploration seismology. It aims to find the optimal reflectivity model in an iterative way. Theoretically, such an inversion imaging method can greatly improve the imaging quality in terms of resolution and signal-to-noise ratio (SNR) compared to the conventional migration imaging method. Dai and Schuster (2009) first realized LSM based on reverse time migration (RTM), known as least-squares reverse time migration (LSRTM). To increase computational efficiency and expedite convergence, they adopted the multisource optimization technique. Since then, LSRTM has been extensively investigated between academia and industry (Tang, 2009; Wong et al., 2010; Dai et al., 2011; Wong et al., 2011; Dai et al., 2012; Dong et al., 2012), thanks to its rigorous theory and competitive imaging results. To adapt to different types of earth media, investigators have proposed elastic LSRTM (Chen and Sacchi, 2017; Duan et al., 2017; Feng and Schuster, 2017; Gu et al., 2017), visco-acoustic LSRTM (Dutta and Schuster, 2014; Sun et al., 2016; Guo and Mcmechan, 2018), and anisotropic LSRTM (Huang et al., 2016; Huang et al., 2017; Qu et al., 2017; Yang et al., 2019). Meanwhile, many optimization techniques are employed further to improve LSRTM, such as plane-wave prestack parameterization to reduce the dependency on the accuracy of the velocity model (Dai and Schuster, 2013), and the inclusion of the information of multiples to supplement subsurface illumination (Wong et al., 2015). Besides, different optimization schemes can be used, including the steepest descent method, conjugate gradient method, parabolic fitting method, and L-BFGS method (Nocedal, 1980; Hou and Symes, 2016), and different definitions can be formulated, such as L2 norm, hybrid L1/L2 norm, and cross-correlation (Zhang et al., 2015; Gu et al., 2017).

However, to our knowledge, few studies on LSRTM in anisotropic media are conducted, and most of them focus on VTI media rather than TTI media (Huang et al., 2016; Huang et al., 2017; Qu et al., 2017; Yang et al., 2019). Two major difficulties hamper the implementation and application of LSRTM in anisotropic media.

One difficulty with PA-LSRTM is its heavy dependency on model parameter errors, in addition to expensive computational cost and slow convergence rate. In the presence of strong anisotropy, this problem will become particularly severe such that the iteration is likely to fail to converge (Huang et al., 2016). Therefore, to ensure the success of LSRTM in anisotropic media, the errors of model parameters (including velocity and anisotropic parameters) have to be relatively small, limiting its application. Dai and Schuster (2013) introduced the prestack parameterization in the plane-wave domain to improve the robustness of LSRTM to velocity errors. Liu et al. (2013) used the extended offset domain and the space shift imaging condition to adapt to glaring velocity errors. Hou and Symes (2016) further speeded up the convergence by applying the weighted conjugate gradient algorithm. In VTI media, Huang et al. (2016) developed an accelerated PA-LSRTM using the plane-wave encoding method, but the strong sensitivity to model parameters errors remains to be solved.

Another difficulty is the evident qSV-wave artefacts. When using the pseudo-acoustic wave equation in anisotropic media, the residual qSV-waves always appear, accompanied by numerical dispersion caused by a low qSV-wave velocity. In the case of TTI media, simulation becomes unstable, especially in areas where the tilt abruptly changes (Zhang et al., 2011), so that the amplitude of some seismic waves is too large to recognize the true seismic wave. LSM, based on the pseudo-acoustic wave equation, suffers from the qSV-wave artefacts (Huang et al., 2017), making the iteration progress unstable. Mathematically, twice square operations on the qP-wave dispersion relation (i.e., phase velocity) produce one extraneous root: the qSV-wave artefact (Chu et al., 2013; Xu and Zhou, 2014). In VTI media, after the acoustic approximation (Alkhalifah, 1998), the extraneous root is the group velocity curve of qSV-wave, manifesting as a diamond-shaped wavefront. In order to accurately simulate pure qP-wave in TTI media, Zhan et al. (2012, 2013) further simplified the phase velocity formula and derived the pure qP-wave governing equation without qSV-wave interference. However, it is difficult to numerically solve this decoupled equation expressed by pseudo-differential operators in the time-space domain. Alternatively, Song et al. (2016) used the function fitting to approximate the root term of the qP-wave phase velocity, but large errors in some phase angle intervals still exist, and the method is hard to be extended to TTI media.

To overcome the limitations of the pseudo-acoustic wave equation, Song and Alkhalifah (2013) used the low-rank approximation approach (Fomel et al., 2010, 2013) to handle the mixed domain operator in orthorhombic media. Without approximating the qP-wave dispersion relation, this method successfully avoids the qSV-wave artifacts and

accurately keeps the kinematical features of seismic waves. By combining low-rank approximation with finite-difference representation, Song et al. (2013) designed a low-rank finite difference (LFD) scheme, and demonstrated that their method could efficiently yield accurate wavefields in TTI media. Therefore, to implement the anisotropic LSRTM, the flexible and efficient LFD method is preferred to derive pure qP-wave linearized forward modeling and migration operators in anisotropic media.

Although the LFD approach has been used in the forward modeling (Song et al., 2013), it is as yet undiscussed in LSRTM. In this study, we apply the LFD approach into the wavefield forward and reverse extrapolation in TTI media and develop pure qP-wave prestack plane-wave LSRTM (LFD-Pre-PLSRTM). Specifically, we first derive pure qP-wave linearized forward modeling and migration operators based on LFD. Such operators can avoid problems related to the pseudo-acoustic wave equation and improve the accuracy and stability of the wavefield in anisotropic media (Huang et al., 2017). Then, in the framework of least-squares migration, we implement pure qP-wave LFD-LSRTM in TTI media. Although the wavefield extrapolator of LFD is quite efficient, the computational cost of LSRTM is still relatively high, especially for the 3D problem. As a result, we introduce the prestack plane-wave strategy into LSRTM, which also can reduce the dependency on the model parameter errors and increase the tolerance to the data noise.

This paper is organized as follows. First, we briefly review the wavefield extrapolator with a low-rank finite difference (LFD) approach. Then, pure qP-wave linearized forward modeling and migration operators are derived. Next, pure qP-wave LFD-Pre-PLSRTM is developed together with the prestack plane-wave strategy. Finally, two numerical examples illustrate that the proposed method can image the complex TTI media accurately and efficiently, even with model parameter errors and data noise.

THEORY

Wavefield extrapolator in anisotropic media using LFD

Before introducing LFD, we begin with the low-rank approximation (Song and Alkhalifah, 2013).

When velocity and anisotropic parameters vary in space, wavefield extrapolation in time can be approximately characterized by a phase operator in the mixed space-wavenumber domain, which can be written as

$$\bar{p}(\mathbf{k}, t + \Delta t) = e^{\pm i|\mathbf{k}|v(\mathbf{x})\Delta t} \bar{p}(\mathbf{k}, t) \quad , \quad (1)$$

where t is time, Δt denotes small time step, $\mathbf{x} = (x, y, z)$ is space vector, $\mathbf{k} = (k_x, k_y, k_z)$ is wave vector, $\bar{p}(\mathbf{k}, t)$ is the Fourier transform of pure qP-wave $p(\mathbf{x}, t)$, $v(\mathbf{x})$ is the wave velocity, and i is the imaginary unit.

Using the inverse Fourier transform for eq. (1), the well-known second-order time-marching scheme can be derived as

$$p(\mathbf{x}, t + \Delta t) + p(\mathbf{x}, t - \Delta t) = 2 \int_{-\infty}^{+\infty} \bar{p}(\mathbf{x}, t) \cos(|\mathbf{k}|v(\mathbf{x})\Delta t) e^{-i\mathbf{k}\cdot\mathbf{x}} d\mathbf{k} \quad , \quad (2)$$

where the mixed domain operator $\cos(|\mathbf{k}|v(\mathbf{x})\Delta t)$ actually describes the propagation behavior of the pure qP-wave.

We call the mixed domain operator the pure qP-wave propagator matrix, and define it as

$$\mathbf{W}(\mathbf{x}, \mathbf{k}) = \cos(|\mathbf{k}|v(\mathbf{x})\Delta t) \quad . \quad (3)$$

According to the low-rank approximation (Fomel et al., 2010, 2013), the propagator matrix (3) can be efficiently decomposed into the following three parts:

$$\mathbf{W}(\mathbf{x}, \mathbf{k}) \approx \sum_{m=1}^M \sum_{n=1}^N \mathbf{W}_1(\mathbf{x}, \mathbf{k}_m) a_{mn} \mathbf{W}_2(\mathbf{x}_n, \mathbf{k}) \quad , \quad (4)$$

where \mathbf{W}_1 and \mathbf{W}_2 are referred to be the submatrices of the propagator matrix \mathbf{W} . \mathbf{W}_1 is constructed by M linearly independent column vectors in \mathbf{W} , and \mathbf{W}_2 is comprised of N linearly independent row vectors in \mathbf{W} . The weighted coefficient a_{mn} connecting \mathbf{W}_1 and \mathbf{W}_2 constitutes a coefficient matrix, which actually determines the effectiveness of decomposition.

As a result, the wavefield extrapolation in time given in the eq. (2) can be sped up by the low-rank approximation (4), leading to

$$p(\mathbf{x}, t + \Delta t) + p(\mathbf{x}, t - \Delta t) \approx 2 \sum_{m=1}^M \mathbf{W}_1(\mathbf{x}, \mathbf{k}_m) \left(\sum_{n=1}^N a_{mn} \left(\int_{-\infty}^{+\infty} \mathbf{W}_2(\mathbf{x}_n, \mathbf{k}) \bar{p}(\mathbf{x}, t) e^{-i\mathbf{k}\cdot\mathbf{x}} d\mathbf{k} \right) \right) \quad , \quad (5)$$

which requires N inverse Fourier transforms at each time extrapolation, thereby directly influencing the computational cost.

To further reduce the computational cost, Song et al. (2013) gave a new finite-difference scheme to solve the eq. (5), which is called the LFD method. Then, the calculation of wavefield $p(\mathbf{x}, t + \Delta t)$ can be rewritten as

$$p(\mathbf{x}, t + \Delta t) + p(\mathbf{x}, t - \Delta t) = \sum_{l=1}^L \mathbf{G}(\mathbf{x}, \boldsymbol{\xi}_l) [p(\mathbf{x}_L, t) + p(\mathbf{x}_R, t)] + \delta(\mathbf{x} - \mathbf{x}_s) f(t) \quad , \quad (6)$$

where $f(t)$ is the time function of the source wavelet, \mathbf{x}_s is the source position, $\delta(\mathbf{x})$ is Dirac function, and $\mathbf{x}_L = (x - \xi_l^x \Delta x, y - \xi_l^y \Delta y, z - \xi_l^z \Delta z)$, $\mathbf{x}_R = (x + \xi_l^x \Delta x, y + \xi_l^y \Delta y, z + \xi_l^z \Delta z)$; $\boldsymbol{\xi}_l = (\xi_l^x, \xi_l^y, \xi_l^z)$ is an integer vector including zero vector, which denotes the position of the l th point in the LFD stencil, and $\mathbf{G}(\mathbf{x}, \boldsymbol{\xi}_l)$ stores each LFD weighted coefficients in this

stencil; L is the size of LFD stencil, which depends entirely upon the order of LFD to be adopted.

Even in TTI media, it only requires to know the propagator matrix \mathbf{W} and then calculate the corresponding LFD coefficient \mathbf{G} , and there is no need to derive the complex explicit wave equation for the pure qP-wave. According to the eq. (3), the propagator matrix \mathbf{W} can be obtained as long as dispersion relation $\omega = |\mathbf{k}|v(\mathbf{x})$ is known. Using the LFD method, it is possible to directly solve the exact dispersion relation instead of the one under acoustic approximation (Alkhalifah, 1998). The accurate dispersion relation of the pure qP-wave in TTI media can be expressed as

$$\omega_{qP} = \sqrt{\frac{1}{2}[(v_h^2 + v_s^2)\hat{k}_h^2 + (v_v^2 + v_s^2)\hat{k}_z^2] + \frac{1}{2}\sqrt{[(v_h^2 - v_s^2)\hat{k}_h^2 - (v_v^2 - v_s^2)\hat{k}_z^2]^2 + 4(v_v^2 - v_s^2)[v_{nmo}^2 - v_s^2]\hat{k}_h^2\hat{k}_z^2}}, \quad (7)$$

where v_h is the qP-wave phase velocity in the isotropic plane (i.e., symmetry plane), v_v is the qP-wave phase velocity along the symmetry axis, v_s is the qS-wave phase velocity along the symmetry axis, v_{nmo} is the qP-wave normal moveout (NMO) velocity, ε and δ are Thomsen parameters characterizing anisotropy (Thomsen, 1986). $\hat{k}_h = \sqrt{\hat{k}_x^2 + \hat{k}_y^2}$ and \hat{k}_z are the horizontal and vertical wavenumbers expressed in a rotated coordinate system aligned with the symmetry axis based on the following transformation:

$$\begin{pmatrix} \hat{k}_x \\ \hat{k}_y \\ \hat{k}_z \end{pmatrix} = \begin{pmatrix} \cos\phi\cos\theta & \sin\phi\cos\theta & -\sin\theta \\ -\sin\phi & \cos\phi & 0 \\ \cos\phi\sin\theta & \sin\phi\sin\theta & \cos\theta \end{pmatrix} \begin{pmatrix} k_x \\ k_y \\ k_z \end{pmatrix}, \quad (7)$$

where θ is the tilt angle of the TTI symmetry axis relative to the vertical axis, ϕ is the azimuth of the TTI symmetry axis which is an angle between the projection of the TTI symmetry axis on xy-plane and x-axis.

For brevity, the wavefield extrapolation given by the equation (6) can be expressed in matrix notations as

$$\mathbf{d} = \mathbf{A}\mathbf{m}, \quad (8)$$

where \mathbf{m} denotes discretized velocity and anisotropic parameters in the model space; \mathbf{d} is the seismic data in the data space; \mathbf{A} represents a full-wave forward modeling operator implemented by the LFD method, which describes the process mapping the model space into the data space.

Pure qP-wave linearized forward modeling and migration operators using LFD

Given the reference models (including the qP-wave phase slowness s_{p0} and anisotropic parameters), the coefficient matrix \mathbf{G}_0 in the LFD stencil is determined. According to the eq. (6), the reference wavefield $p_0(\mathbf{x}, t + \Delta t)$ can be given by

$$p_0(\mathbf{x}, t + \Delta t) = -p_0(\mathbf{x}, t - \Delta t) + \sum_{l=1}^L \mathbf{G}_0(\mathbf{x}, \xi_l) [p_0(\mathbf{x}_L, t) + p_0(\mathbf{x}_R, t)] + \delta(\mathbf{x} - \mathbf{x}_s) f(t). \quad (9)$$

Defining the true slowness perturbation model (i.e., reflectivity model) as

$$\mathbf{m}(\mathbf{x}) = \frac{s_p^2 - s_{p0}^2}{s_{p0}^2} = \frac{\Delta s_p^2}{s_{p0}^2}, \quad (10)$$

where s_p stands for the true slowness model, Δs_p is the perturbation slowness model. Based on the seismic wave perturbation theory and Born approximation, we can derive the wavefield forward extrapolation formula

$$p_s(\mathbf{x}, t + \Delta t) = -p_s(\mathbf{x}, t - \Delta t) + \sum_{l=1}^L \mathbf{G}_0(\mathbf{x}, \xi_l) [p_s(\mathbf{x}_L, t) + p_s(\mathbf{x}_R, t)] + \mathbf{m}(\mathbf{x}) \cdot \frac{\partial p_0(\mathbf{x}, t)}{\partial t}, \quad (11)$$

where p_s is the perturbation wavefield.

In a compact form, the linearized forward modeling operator (11) can be formulated as

$$\mathbf{d}^{cal} = \mathbf{Lm}, \quad (12)$$

where \mathbf{m} is the imaging result of each iteration in LSRTM, \mathbf{d}^{cal} is the calculated seismic data using linearized forward modeling operator \mathbf{L} .

As a result, migration operator can be derived from linearized forward modeling operator by the adjoint-state method (Plessix, 2006), and the adjoint wavefield p^* can be reconstructed as

$$p^*(\mathbf{x}, t - \Delta t) = -p^*(\mathbf{x}, t + \Delta t) + \sum_{l=1}^L G_0(\mathbf{x}, \xi_l) [p^*(\mathbf{x}_L, t) + p^*(\mathbf{x}_R, t)], \quad (13)$$

$$p^*(\mathbf{x}, t) = \delta(\mathbf{x} - \mathbf{x}_g) d(\mathbf{x}_g, t; \mathbf{x}_s)$$

where $d(\mathbf{x}_g, t; \mathbf{x}_s)$ is the seismic data observed by a receiver at \mathbf{x}_g due to a source excitation at \mathbf{x}_s . On the contrary to the source wavefield p_0 shown in the eq. (9), the receiver wavefield p^* is the back extrapolation in time. Note that calculations of both wavefields adopt the identical LFD coefficient matrix \mathbf{G}_0 .

Finally, by applying the imaging condition that is a zero-lag cross-correlation between the second-order time partial derivative of the source wavefield and receiver wavefield, the imaging result $\mathbf{m}(\mathbf{x}; \mathbf{x}_s)$ is expressed as

$$\mathbf{m}(\mathbf{x}; \mathbf{x}_s) = \int_t s_{p0}^2 \cdot \frac{\partial^2 p_0(\mathbf{x}, t)}{\partial^2 t} \cdot p^*(\mathbf{x}, t). \quad (14)$$

Equally, the imaging process denoted by (13) and (14) can be compactly expressed as:

$$\mathbf{m}_{mig} = \mathbf{L}^T \mathbf{d}^{obs}, \quad (15)$$

where \mathbf{L}^T is the migration operator, and \mathbf{m}_{mig} is the imaging result for a single shot data. In RTM, \mathbf{d}^{obs} represents the observed data, whereas in the LSRTM, \mathbf{d}^{obs} is usually the residual between the observed data and the calculated data and \mathbf{m}_{mig} is the gradient model to update the image in each iteration.

Pure qP-wave LFD-LSRTM and prestack plane-wave strategy

For the standard LSRTM, the objective function in the shot domain can be written as

$$J(\mathbf{m}) = \frac{1}{2} \sum_{i=1}^{N_s} \left\| \mathbf{L}_i \mathbf{m} - \mathbf{d}_i^{obs} \right\|_2^2 \rightarrow \min, \quad (16)$$

where N_s is the total number of shot gathers, $\|*\|_2$ stands for the L_2 norm, and \mathbf{m} is the final reflectivity model.

The implementation of the pure qP-wave LFD-LSRTM can be depicted by the flowchart shown in Fig. 1. In contrast to the acoustic wave LSRTM in isotropic media, our method mainly differs in the steps denoted by red boxes, where the linearized forward modeling and migration operators use the LFD method. Therefore, we call our method **LFD-LSRTM**, which can deal with the pure qP-wave in TTI media.

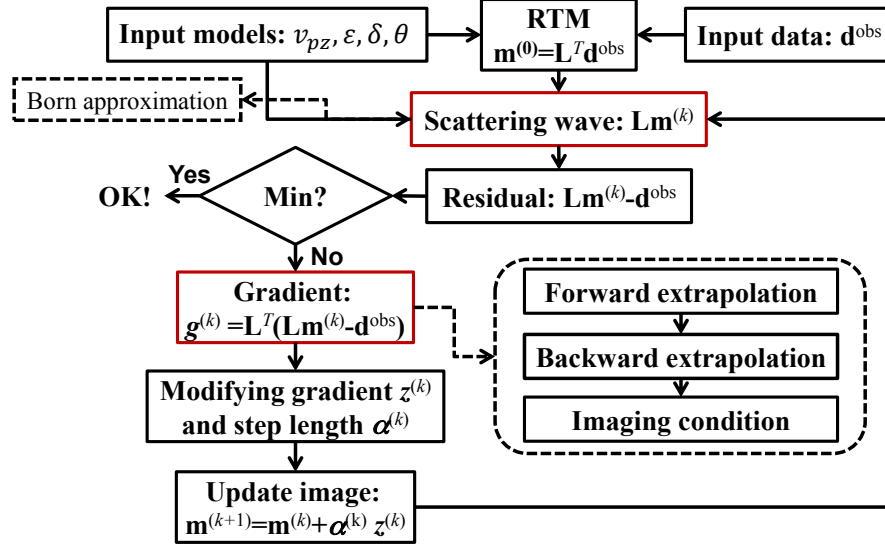


Fig. 1. The flowchart of the numerical implementation of the pure qP-wave LFD-LSRTM.

To further improve the practicality and efficiency, we introduce the prestack plane-wave strategy into the pure qP-wave LFD-LSRTM method, which is referred to be **LFD-Pre-PLSRTM**. The strategy contains two techniques: the plane-wave encoding and the prestack parameterization in the plane-wave domain.

On the one hand, the plane-wave encoding technique can be expressed as

$$d(x_g, t; p) = \sum_{x_s} d(x_g, t; x_s) * \delta(t - p \cdot x_s) \quad , \quad (17)$$

where $d(x_g, t; x_s)$ is the shot-domain data, $d(x_g, t; p)$ is the plane-wave-domain data, also known as the plane-wave gather, $\delta(t - p \cdot x_s)$ is the time-shift function, $*$ denotes the convolution operation, $p \cdot x_s$ is the time shift that is a linear function of the source position x_s . p is the ray parameter which is defined as

$$p = \frac{\sin \theta}{v} \quad , \quad (18)$$

where θ is the incident angle of the plane wave relative to the vertical axis, and v is the velocity near the surface. By choosing N_p different ray parameters p , N_p plane-wave gathers with different incident angles can be obtained.

Using the same encoding function, the plane-wave source wavefield is also constructed. Generally, N_s point sources are encoded into N_p plane-wave sources ($N_p \ll N_s$). Here, we call LFD-LSRTM in plane-wave domain **LFD-PLSRTM**.

On the other hand, the prestack parameterization technique helps LFD-LSRTM greatly enhance the imaging robustness even in the presence of errors in the reference models or/and noise in the seismic data. In each iteration, N_p independent gradient models are individually stored, and N_p independent reflectivity models are separately updated. Obviously, the prestack parameterization technique would need slightly extra memory that is proportional to N_p , but this technique enables our method to be feasible for the field data. We call LFD-PLSRTM with the prestack parameterization technique **LFD-Pre-PLSRTM**.

Last, Table 1 lists the computation time and I/O cost for LFD-LSRTM, LFD-PLSRTM, and LFD-Pre-PLSRTM, respectively. We can summarize that (1) the computation time of LFD-PLSRTM and LFD-Pre-PLSRTM is evidently less than that of LFD-LSRTM, which is attributed to the fact of $N_p \ll N_s$; (2) the I/O cost of LFD-Pre-PLSRTM is higher than LSRTM and PLSRTM because of the prestack parameterization technique.

Table 1. Computation time and I/O cost of LFD-LSRTM, LFD-PLSRTM and LFD-Pre-PLSRTM for 2D fixed-spread acquisition geometry.

Method	Computation time (s)	I/O cost ($\times 4$ byte)
LFD-LSRTM	$N_{iter} \times N_s \times (2 \times T_{mod} + T_{rtm})$	$(ng \times nt) + (3 \times nx \times nz) + (nt \times nx \times nz) + (6 \times nx \times nz)$ Shot gather + wavefield + forward wavefield + $(2 \times \text{image} + 2 \times \text{gradient} + 2 \times \text{update})$
LFD-PLSRTM	$N_{iter} \times N_p \times (2 \times T_{mod} + T_{rtm})$	$(ng \times nt) + (3 \times nx \times nz) + (nt \times nx \times nz) + (6 \times nx \times nz)$ Shot gather + wavefield + forward wavefield + $(2 \times \text{image} + 2 \times \text{gradient} + 2 \times \text{model})$
LFD-Pre-PLSRTM	$N_{iter} \times N_p \times (2 \times T_{mod} + T_{rtm})$	$(ng \times nt) + (3 \times nx \times nz) + (nt \times nx \times nz) + (6 \times nx \times nz) \times N_p$ Shot gather + wavefield + forward wavefield + $(2 \times \text{image} + 2 \times \text{gradient} + 2 \times \text{model}) \times N_p$

NB: N_{iter} —number of iteration, N_s —number of shot gather, N_p —number of plane-wave gather, T_{mod} —time of linearized forward modeling for one shot gather, T_{rtm} —time RTM for one shot gather, nx and nz —2D model size, nt —number of time samples for each trace, ng —number of traces or receivers for each shot gather.

NUMERICAL EXAMPPLES

Two synthetic examples are used to illustrate the performance of the proposed method.

Salt model

Model parameters

Figs. 2a-d display the true P-wave velocity, migration velocity, and anisotropy parameters for the salt model, respectively. The salt model is discretized with a grid of 676×201 with a spatial interval of 10 m. Its velocity ranges from 1500 m/s to 4482 m/s. Fig. 2e gives the slowness perturbation model defined by the eq. (10).

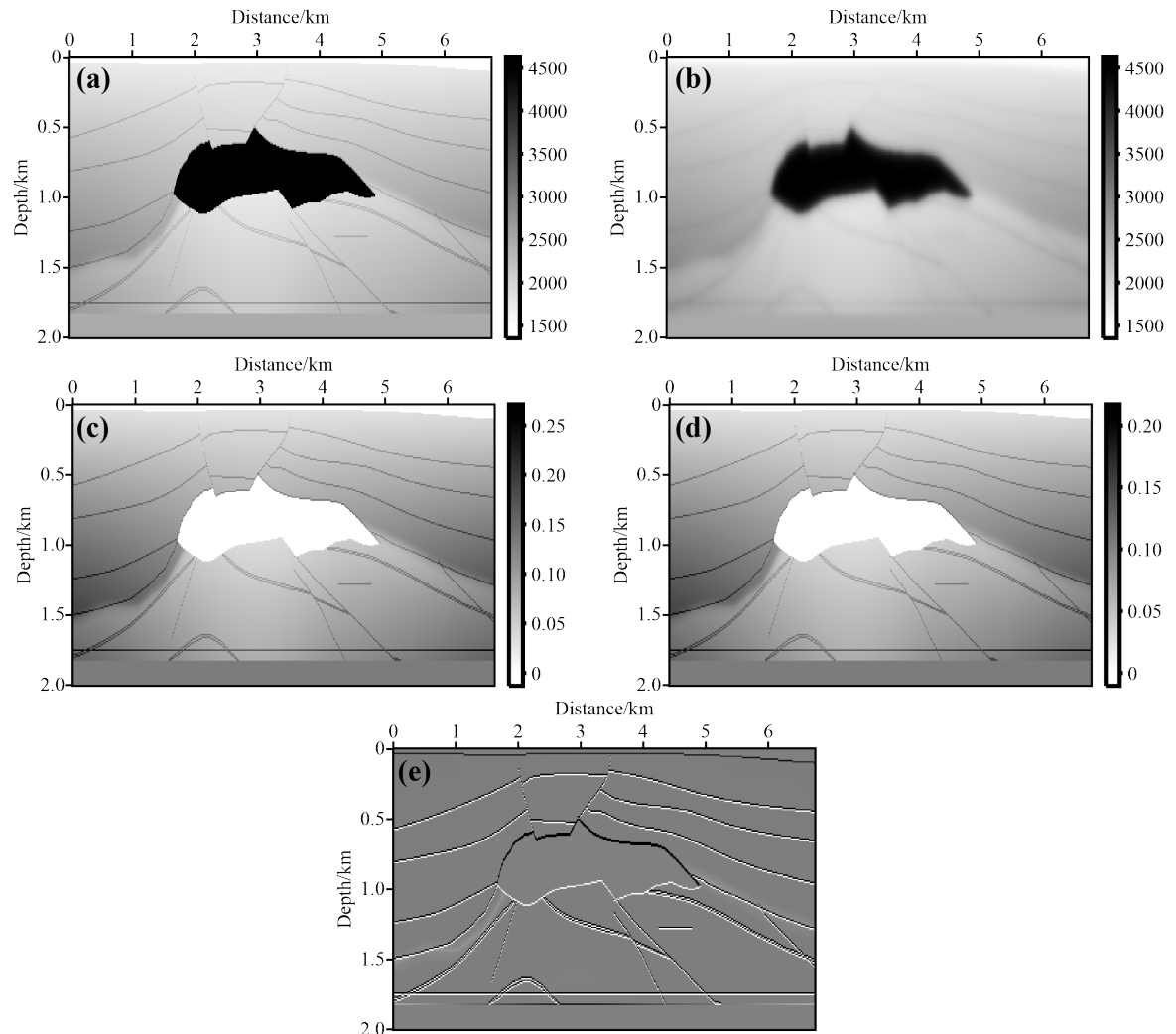


Fig. 2. The Salt model: (a) true P-wave velocity model (unit: m/s), (b) P-wave migration velocity model (unit: m/s), (c) ϵ model, (d) δ model, and (e) true reflectivity model (slowness perturbation model).

Considering the numerical dispersion condition, a 20 Hz Ricker wavelet is used as the source time function. Regarding the acquisition system, 338 shots are evenly deployed at a depth of 20 m with a 20 m spacing, and the first shot is located at the leftmost end of the model. For each shot, 676 receivers are used to record wavefields within a split-spread aperture of 6.75 km. The recording length of each seismogram is 5 s with a time sampling interval of 1 ms. In the light of the model configuration and model parameters shown in Figs. 2b-d, LFD coefficient matrix \mathbf{G} can be calculated.

Analysis of shot gather

The observed shot gather is shown in Fig. 3a. Since it is synthesized by the linearized forward modeling method, the obtained shot gather is the scattered wavefields which contain no direct waves. It can be seen that the coherent events are clear without numerical dispersions. The shot gather using the traditional pseudo-acoustic wave equation is displayed in Fig. 3b. By comparison, we find that shot gathers using two different linearized forward modeling methods have consistent traveltimes, indicating that linearized forward modeling operator using the LFD method can effectively simulate wavefield in the VTI media.

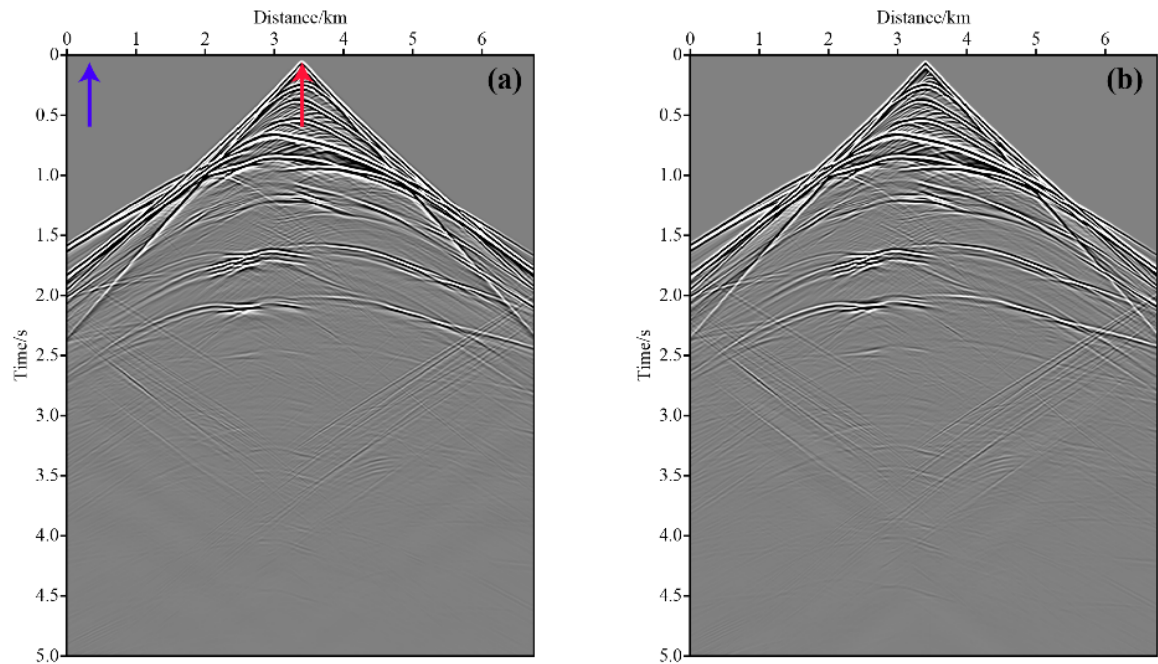


Fig. 3. The linearized forward modeling record using (a) LFD method in VTI media, (b) pseudo-acoustic wave equation in VTI media. The red arrow denotes the near-offset position at CDP 320, and blue arrow denotes the far-offset position at CDP 30.

To observe results in a more detailed way, Fig. 4 shows single-trace records at the near and far offsets, respectively. The near offset is located at CDP 320 (red arrow in Fig. 3a) and far offset at CDP 30 (blue arrow in Fig. 3a). Fig. 4a gives the near-offset single-trace records using the LFD method (red line) and traditional pseudo-acoustic wave equation method (blue line). Two single-trace records basically coincide with each other, which verifies that results at the near offset using the LFD method are correct. Likewise, Fig. 4b corresponding to results at the far offset gives a similar demonstration. In addition, through calculating spectra of the single-trace records in Fig. 3, Fig. 4c shows nearly the same spectra for two different methods for a given medium. This demonstrates the validity of the LFD linearized forward modeling operator.

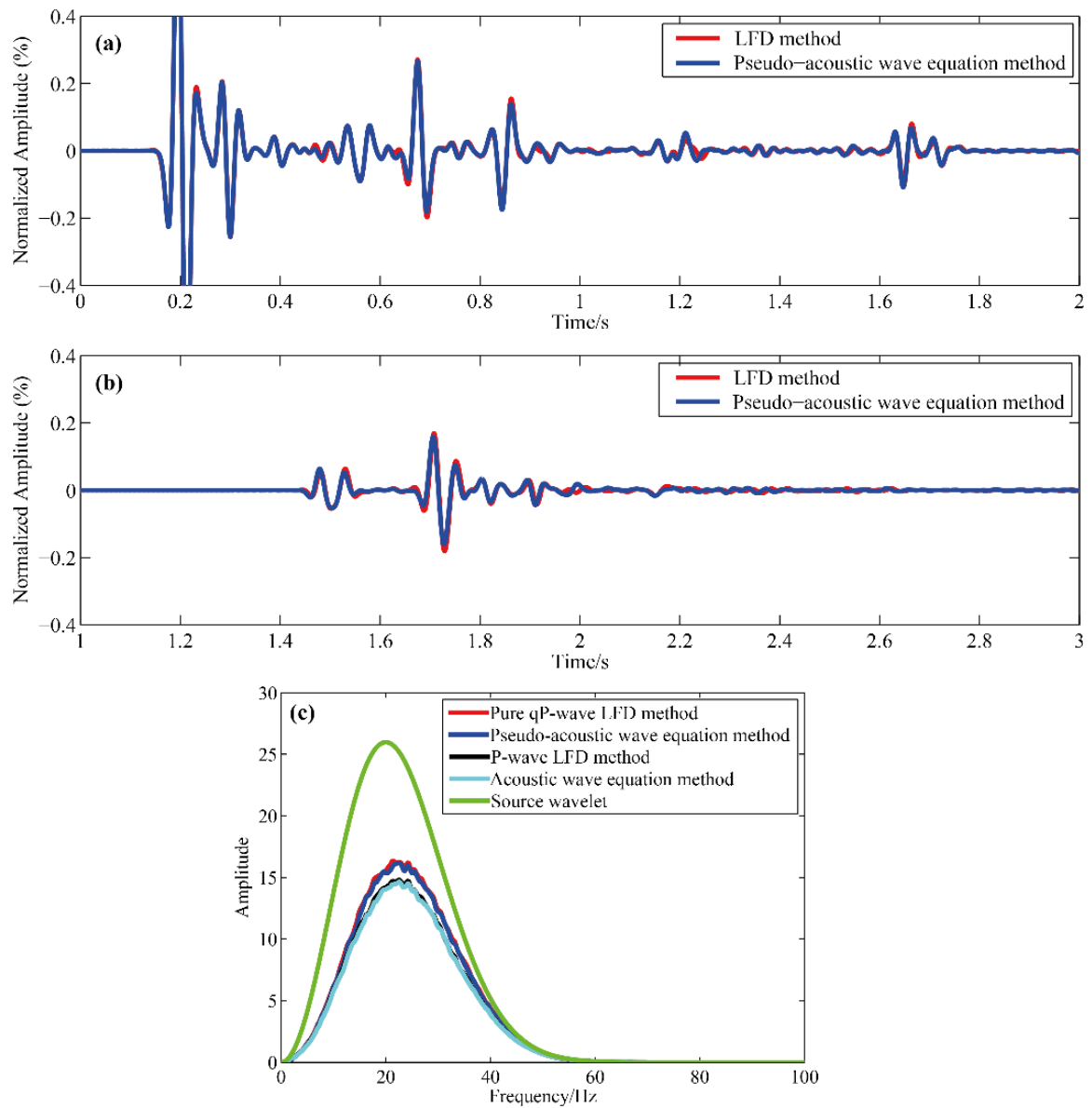


Fig. 4. Comparison of single-trace records in the time and frequency domain, respectively. The single-trace record in VTI media at (a) CDP 320 and (b) CDP 30. (c) Spectra of single-trace records in Fig. 3.

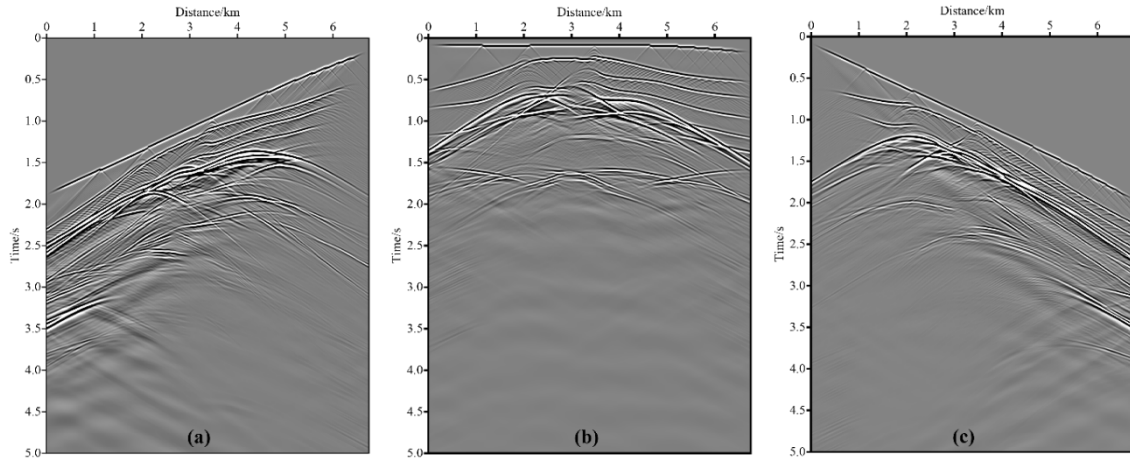


Fig. 5. The plane-wave gathers with ray parameter p as (a) -0.27 s/km, (b) 0 s/km and (c) 0.27 s/km.

To apply the prestack plane-wave strategy, 338 shot gathers are transformed into 31 plane-wave gathers with ray parameter p linearly increasing from -0.27 s/km to 0.27 s/km, according to the eq. (17). Correspondingly, the incident angle of plane wave ranges from -23° to 23° . This strategy enables to reduce the data size to about one-tenth, thereby largely saving memory space, significantly decreasing I/O cost and computational time. Fig. 5 shows three plane-wave gathers with different ray parameters p which are -0.27 s/km, 0 s/km, and 0.27 s/km, separately. The obtained plane-wave gather very resembles the stacked section, especially for the plane-wave gather with $p = 0$ s/km in which the structures near the surface can be roughly identified (Fig. 5b). The deep layers or complex structures, however, are difficult to be recognized in the plane-wave gather, so migration methods are needed to recover the reflected energy and converge the diffracted energy.

Comparison of imaging results

Figs. 6a and b are the results of LFD-LSRTM after 1 and 30 iterations, respectively. Similar to the image of RTM, Fig. 6a suffers from the severe low-frequency noise, especially for the near-surface region and the top and bottom of the salt body. Moreover, strong energy appears at the source positions, and the deep layer shows poor continuity and relatively weak imaging energy. After 30 iterations, LFD-LSRTM however yields an excellent imaging result (Fig. 6b). Specifically, the low-frequency noise is successfully removed, the source effect disappears, and energy in the middle-deep layer is well enhanced, making amplitudes of the entire image more balanced. This confirms that the quality of the inversion imaging is obviously better than the migration imaging. Meanwhile, Fig. 6c gives the result of PA-LSRTM after 30 iterations. By comparison, LFD-LSRTM shows a high agreement with PA-LSRTM, verifying that the proposed method is reasonable.

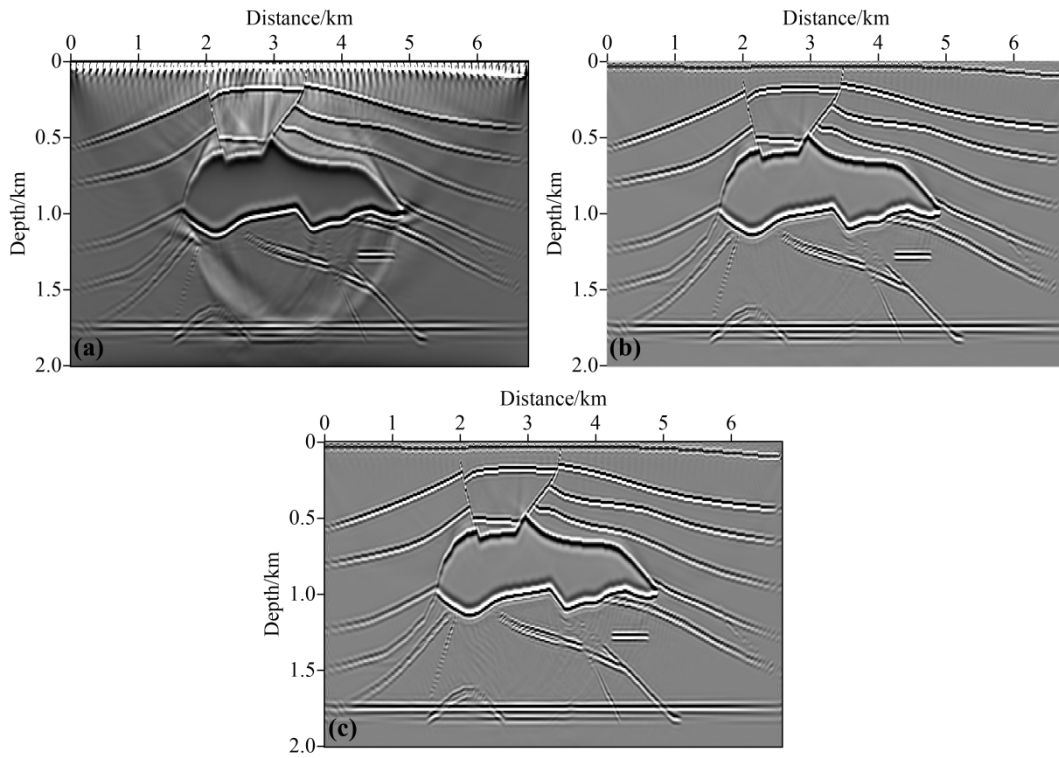


Fig. 6. Shot-domain LFD-LSRTM image after (a) 1 iteration and (b) 30 iterations. (c) Shot-domain PA-LSRTM image after 30 iterations.

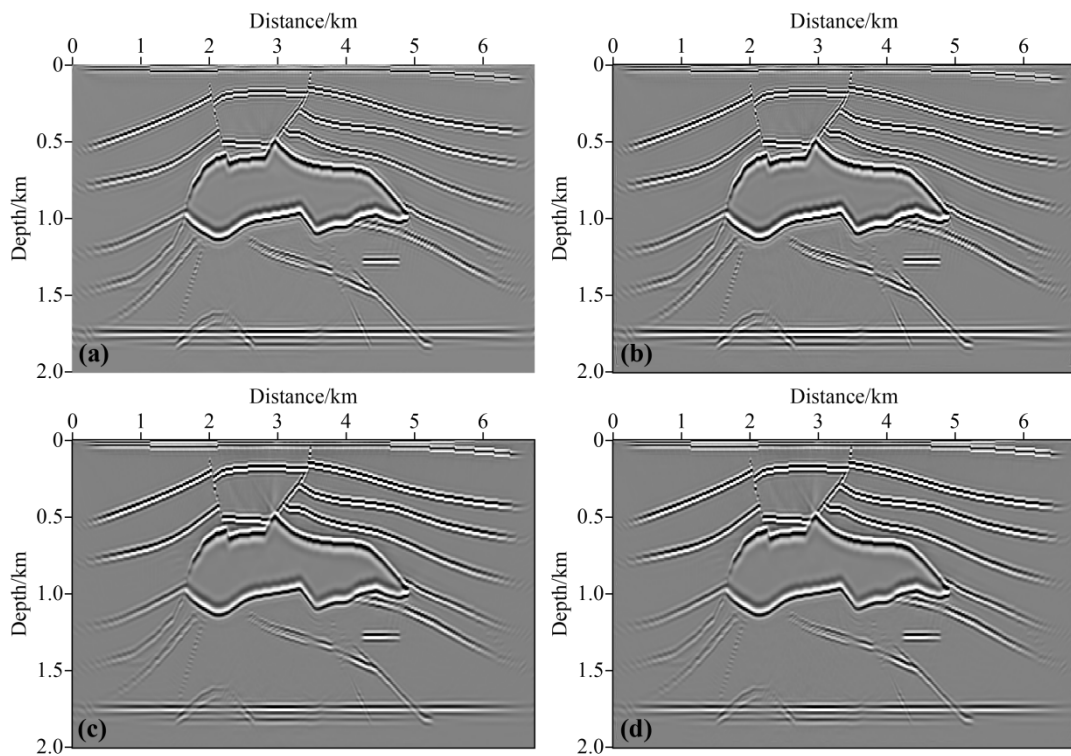


Fig. 7. Plane-wave domain inversion images after 30 iterations using (a) LFD-PLSRTM method, (b) PA-PLSRTM method, (c) LFD-Pre-PLSRTM method and (d) PA-Pre-PLSRTM method.

Fig. 7 compares the imaging results of four different plane-wave LSRTM methods. The greatest advantage of the plane-wave LSRTM is that it reduces its computational cost to one-tenth of that in the shot domain but yields a satisfactory imaging result (comparing Figs. 7a and 7c with Fig. 6b, or comparing Figs. 7b and 7d with Fig. 6c). It can be seen that LSRTM with the prestack plane-wave strategy shows a higher convergence rate, so for the same number of iterations, the method with prestack plane-wave strategy has a higher image quality than the method with the plane-wave strategy.

Moreover, Table 2 summarizes the CPU computational time and I/O cost of one iteration of different methods. By comparison, LFD-Pre-PLSRTM spends the least computational time to achieve an acceptable result but with similar I/O cost.

Table 2. CPU computational time and I/O cost for one iteration of different methods when using a single node on the same workstation.

Methods	LFD-LSRTM	LFD-PLSRTM	LFD-Pre-PLSRTM	PA-LSRTM	PA-PLSRTM	PA-Pre-PLSRTM
Computational time (hours)	15.773	1.533	1.495	48.446	4.725	4.677
I/O cost (GB)	2.549	2.527	2.695	2.785	2.802	2.965

Tests with noise data

In the previous results, the data is free of noise. Unfortunately, the data is always contaminated by stochastic or/and coherent noise in real cases. To test the effectiveness of LFD-Pre-PLSRTM in the presence of the noise, three different levels of stochastic noise are added into the above 31 plane-wave gathers to produce the data set with S/N of 2, 1, and 0.5, respectively (see Figs. 8a-c). For comparison, LFD-PLSRTM is also investigated.

The imaging results using the data with the above three S/N ratios are shown in Fig. 9, where Figs. 9a-c use LFD-PLSRTM and Figs. 9d-f use LFD-Pre-PLSRTM. With the decrease of S/N, the imaging quality of both methods becomes worse, because the presence of stochastic artefacts reduces the S/N and resolution of the imaging results. However, complex geological bodies such as salt body and faults, and the bottom flat interface are still clearly imaged and well identified.

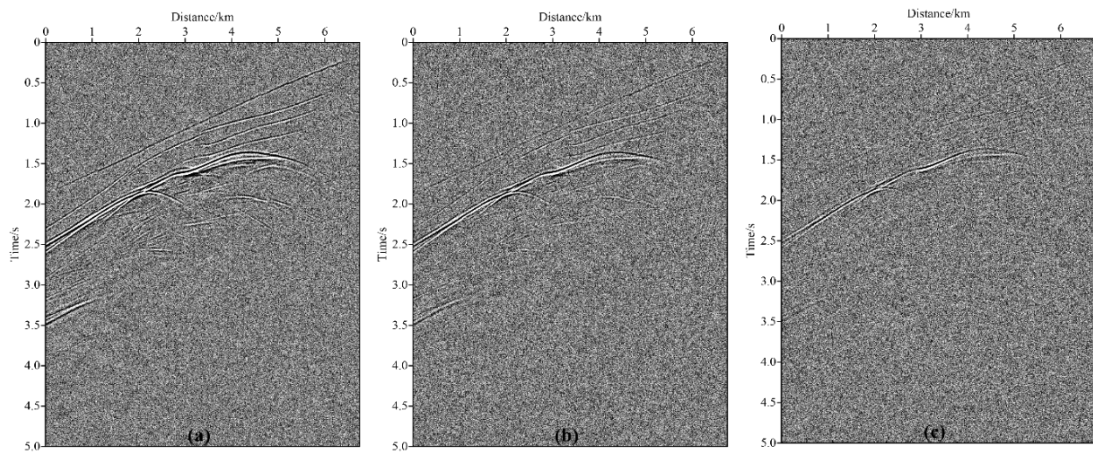


Fig. 8. The plane-wave gather with (a) $S/N = 2$, (b) $S/N = 1$ and (c) $S/N = 0.5$.

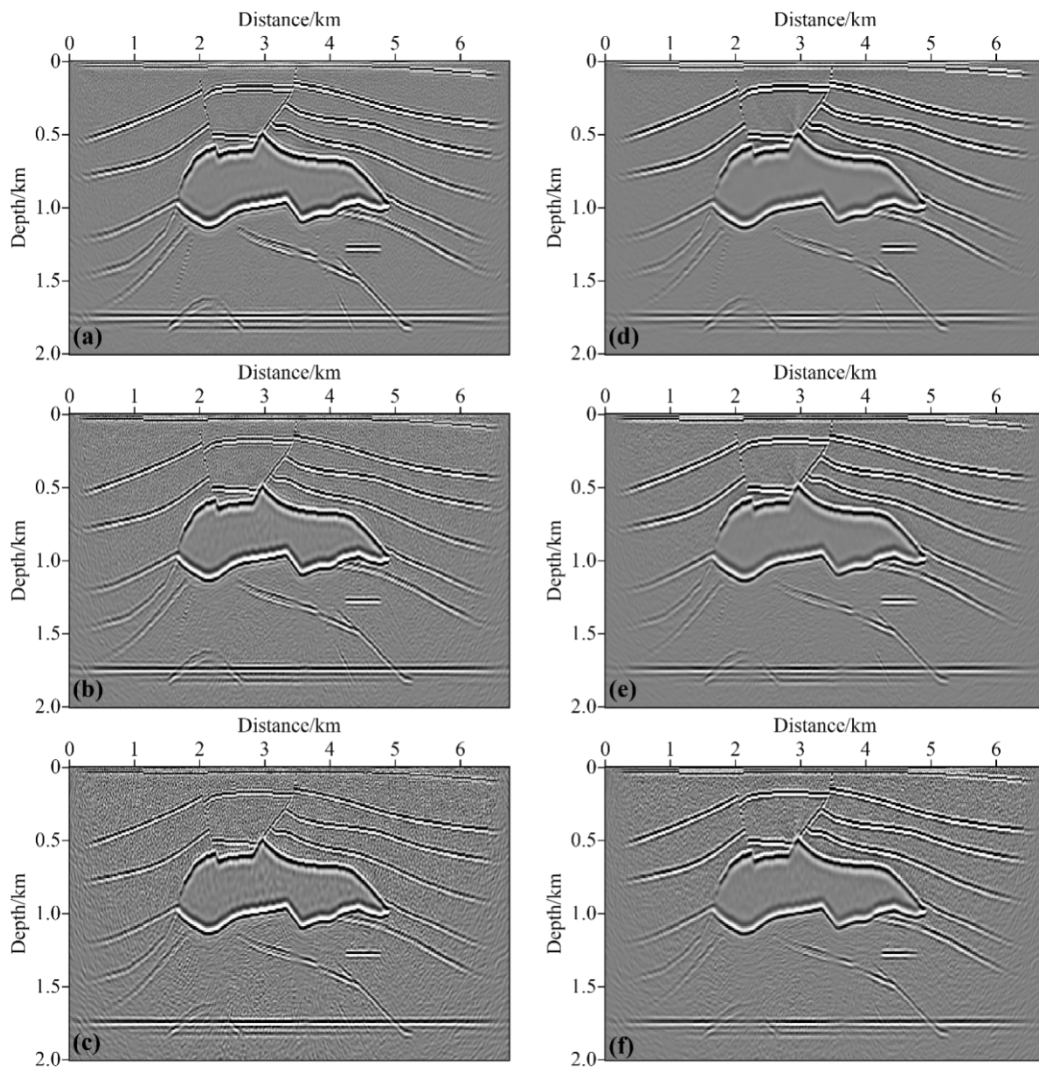


Fig. 9. The plane-wave domain LFD inversion images after 30 iterations. LFD-PLSRTM image using data with (a) $S/N = 2$, (b) $S/N = 1$, and (c) $S/N = 0.5$. LFD-Pre-PLSRTM image using data with (d) $S/N = 2$, (e) $S/N = 1$, and (f) $S/N = 0.5$.

Marmousi2 model

To further test the adaptability of the proposed method in complex structures, the Marmousi2 model is investigated.

Model parameters

The modified Marmousi2 model is shown in Fig. 10. Fig. 10a corresponds to the true P-wave velocity model. Note that there is a low-speed anomaly at (3 km, 1.1 km), making the numerical implementation very susceptible to the numerical dispersion. Fig. 10b is the migration velocity. Figs. 10c and 10d are ε and δ models, respectively.

The model consists of 1361×351 grid points with a 12.5 m horizontal grid interval and a 10 m vertical grid interval. The velocity varies from 1028 m/s to 4700 m/s. Considering the stability condition and computational efficiency, the time sampling interval is 1 ms and the recording length is 7 s. Combining these model parameters with the choice of 8th-order LFD stencil, the LFD coefficient matrix can be calculated.

The synthetic data has a total of 681 shot gathers with a shot interval of 25 m at a depth of 20 m, which are generated by a Ricker wavelet with a dominant frequency of 18 Hz. The first shot excites at the leftmost end of the model, and each shot is recorded by 1361 receivers with a receiver interval of 12.5 m.

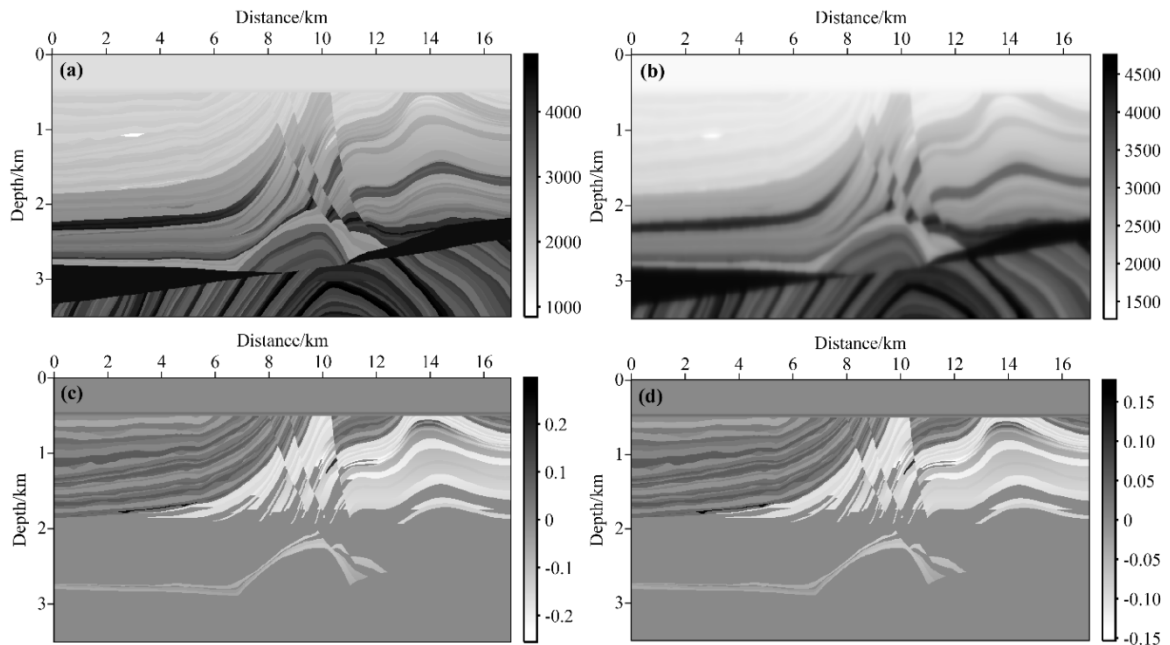


Fig. 10. The modified Marmousi2 model: (a) true P-wave velocity model (unit: m/s), (b) P-wave migration velocity model (unit: m/s), (c) ε model, and (d) δ model.

Analysis of shot gather

Fig. 11a is one shot record calculated by the LFD linearized forward modeling operator. At the same shot position, Fig. 11b gives the shot record simulated by the traditional pseudo-acoustic wave linearized forward modeling operator.

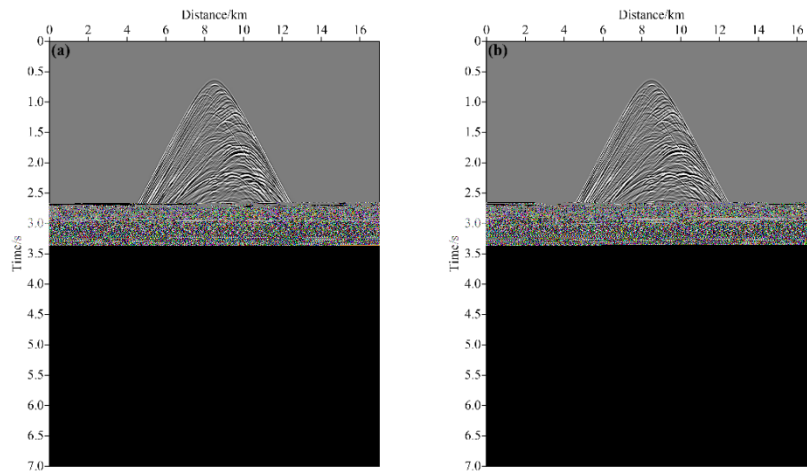


Fig. 11. The linearized forward modeling record using (a) LFD method in VTI media, (b) pseudo-acoustic wave equation in VTI media.

In the same way, 681 shot gathers are transformed into 35 plane-wave gathers with ray parameters evenly changing from -0.2 s/km to 0.2 s/km. Fig. 12 displays the linearized wavefield snapshot at 0.6 s in the plane-wave domain. To illustrate the validity of our method, the snapshot obtained from the traditional pseudo-acoustic wave equation is also given. It can be clearly seen that there is serious noise due to qSV-wave artefacts and instability, as indicated by the red arrows (see Fig. 12a), while the result of our method shows no noise and stays stable (see Fig. 12b).

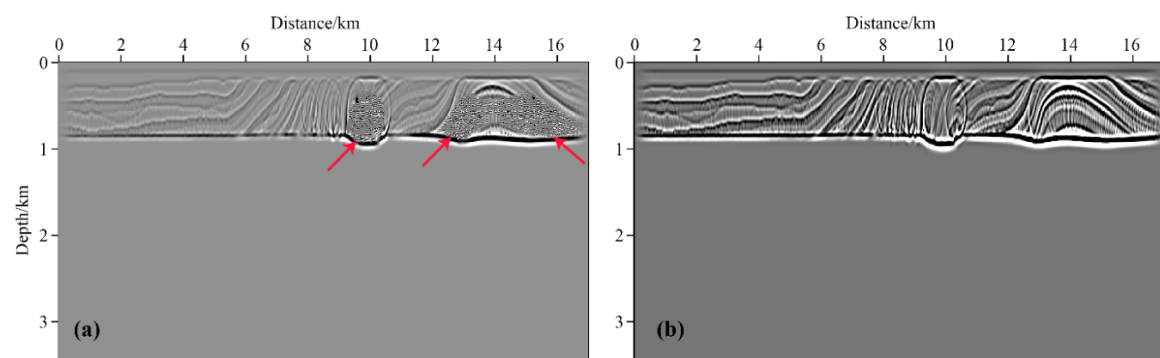


Fig. 12. Comparison of linearized wavefield snapshots at 0.6 s generated from (a) traditional pseudo-acoustic wave equation, (b) LFD linearized forward modeling.

Comparison of imaging results

Figs. 13a-d compares the imaging results without noise in the data. For this complex model, four methods all obtain acceptable results: three significant faults, anticline, unconformity, and steep layers in the deep are clearly imaged. Comparing Figs. 13a with 13b (or Figs. 13c with 13d), whether PA or LFD method is applied, the prestack plane-wave strategy provides a higher image quality than the plane-wave strategy, which can be further verified by the convergence curves in Fig. 14. Comparing Figs. 13a with 13c (or Figs. 13b with 13d), the imaging results are almost the same, which indicates that the proposed method is capable of handling the sophisticated model imaging. In order to check the adaptability of the proposed approach to the noisy data, Figs. 13e and 13f give the results of LFD-PLSRTM and LFD-Pre-PLSRTM when the S/N of the data is 1. We can find that the image S/N is degraded, but the main geological targets are still accurately positioned. In contrast to LFD-PLSRTM, LFD-Pre-PLSRTM shows a better image (Figs. 13e and 13f). In particular, near the anticline's right limb (indicated by the red circle), the image of LFD-PLSRTM is blurred, while LFD-Pre-PLSRTM shows an image as clear as one without the effect of the noise (Fig. 13d), indicating that LFD-Pre-PLSRTM is still feasible for the data containing reasonable noise.

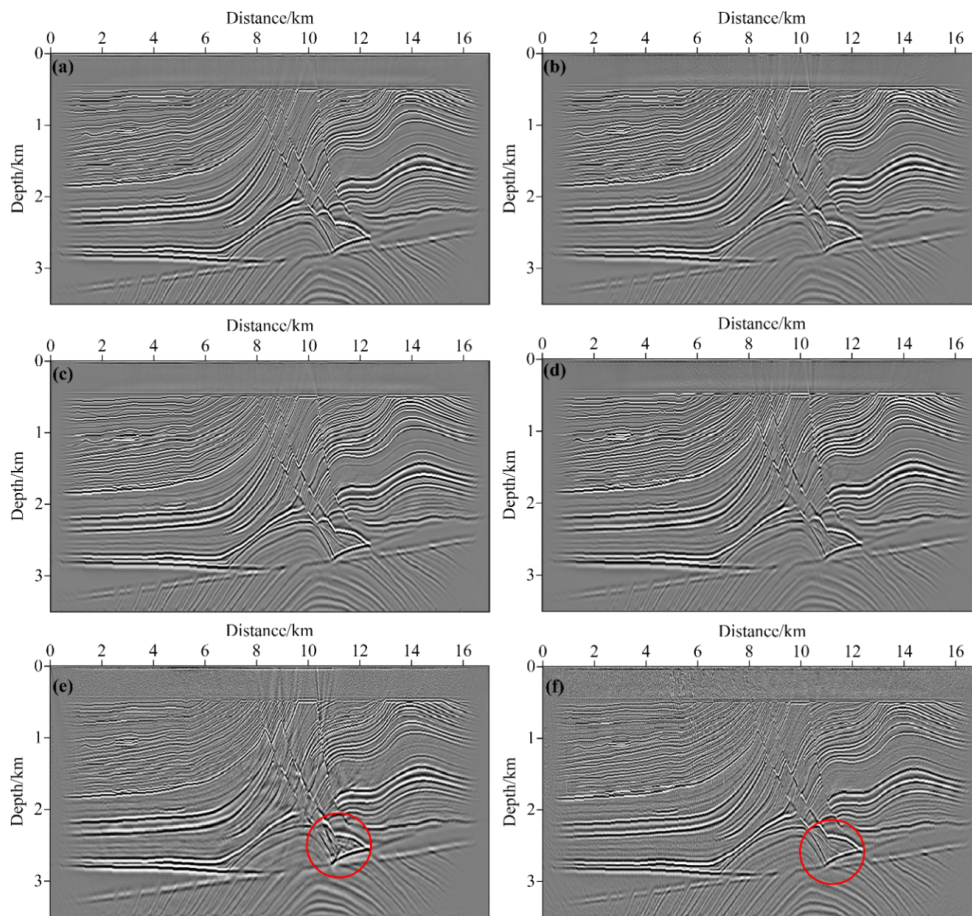


Fig. 13. The inversion images after 30 iterations without noise in data using (a) PA-PLSRTM method, (b) PA-Pre-PLSRTM method, (c) LFD-PLSRTM method and (d) LFD-Pre-PLSRTM method. The inversion images after 30 iterations in the case of S/N = 1 in the data using (e) LFD-PLSRTM method and (f) LFD-Pre-PLSRTM method.

Fig. 14 displays the convergence curves associated with the results shown in Fig. 13. It can be seen that when the data is absent from the noise, Pre-PLSRTM is significantly better than PLSRTM regardless of the inversion imaging method used.

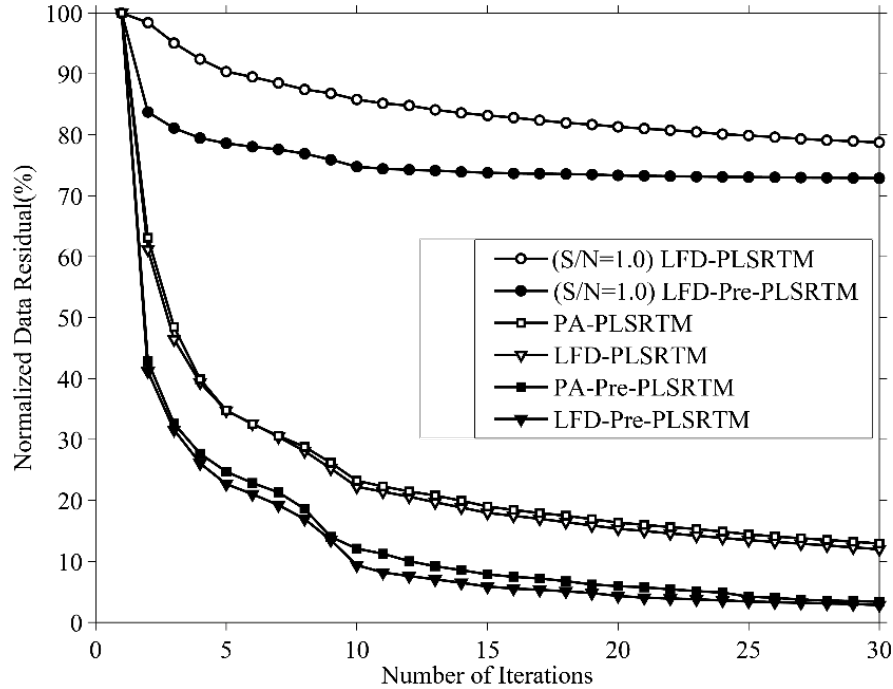


Fig. 14. The curves of the normalized data residual versus the iteration number that correspond to imaging results shown in Fig. 13.

Sensitivity to model parameter errors

To test the robustness of LFD-Pre-PLSRTM to the model parameter errors, we investigate the effects of errors in terms of the velocity model, Epsilon model, Delta model, and tilt angle model, respectively, based on the control variable method. For better comparison, LFD-PLSRTM is discussed as well.

(1) Velocity errors

The results of LFD-Pre-PLSRTM are shown in Fig. 15, which corresponds to the velocity model errors of 0%, 2%, 5%, and 8%, respectively. As the velocity model error increases, the image gradually becomes blurred. When the velocity model error is up to 8% (Fig. 15d), faults and anticline cannot be clearly recognized because diffracted energy fails to be correctly positioned, and high-dip layers in the deep obviously become smeared and weakened. Besides, imaging positions appear a significant deviation along the vertical direction, and this deviation increases with the depth, manifesting as an uneven pull-up. Consequently, the velocity error has a considerable influence on the final imaging quality.

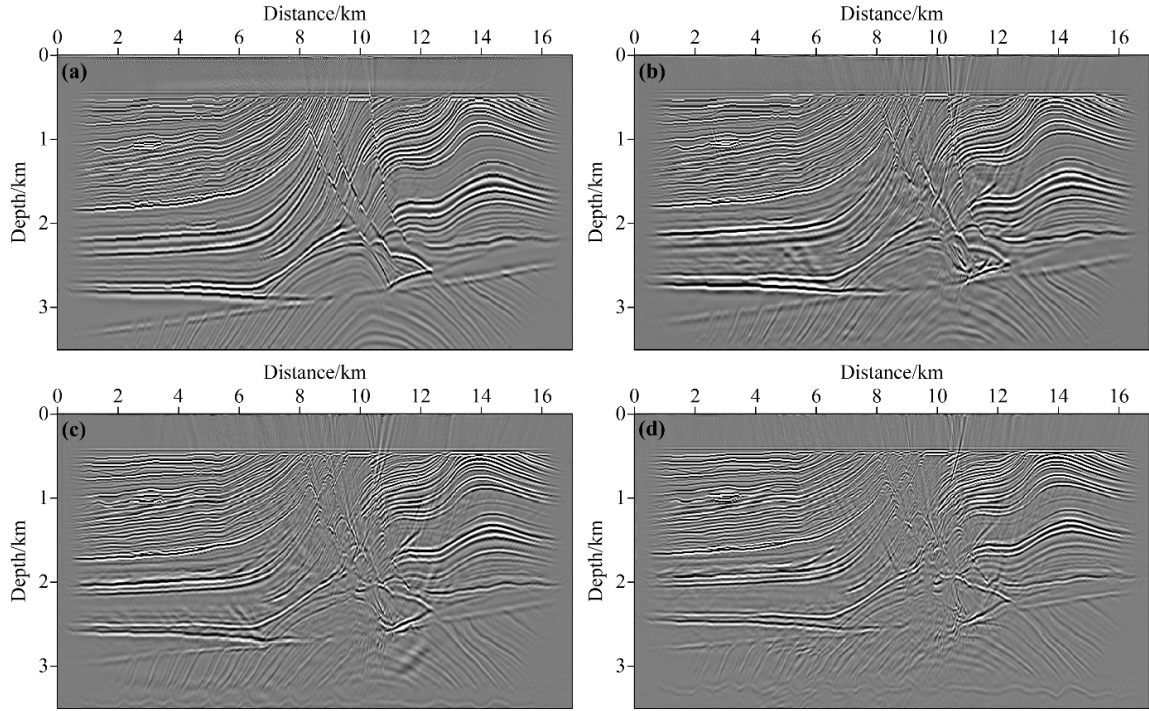


Fig. 15. LFD-Pre-PLSRTM images when using velocity model with errors of (a) 0%, (b) 2%, (c) 5% and (d) 8%.

(2) ε and δ errors

Furthermore, we test the ε with errors of 0%, 8%, 18%, and 28%, and δ with errors of 0%, 8%, 28%, and 48%, respectively. Since ε and δ parameters affect seismic wave velocity in different manners, they should have different sensitivity to the imaging results. Here we no longer show the imaging results, but give data residual convergence curves in Fig. 16. LFD-Pre-PLSRTM has some sensitivity to ε errors but not strong, because the convergence rate decreases slightly with the increase of ε errors (Fig. 16a), and even when ε errors increase to 28%, the data residual can still converge towards a relatively small value (about 25%). It is evident that δ errors have fewer impacts on the convergence than ε errors (Fig. 16b), due to the fact that the convergence for δ errors of 48% is comparable to that for ε errors of 28%.

(3) Tilt angle errors

Figs. 17a-d exhibit the imaging results using tilt angle of 80° (true model), 60° , 30° , and 0° , respectively. When the tilt angle model has errors, complex structures like steep faults and anticline are wrongly positioned events. Also, the image appears strong migration artefacts near the surface. As tilt angle errors increase, these problems become more dominant such that typical structures are hard to be imaged. This illustrates that LFD-Pre-PLSRTM is profoundly sensitive to tilt angle errors.

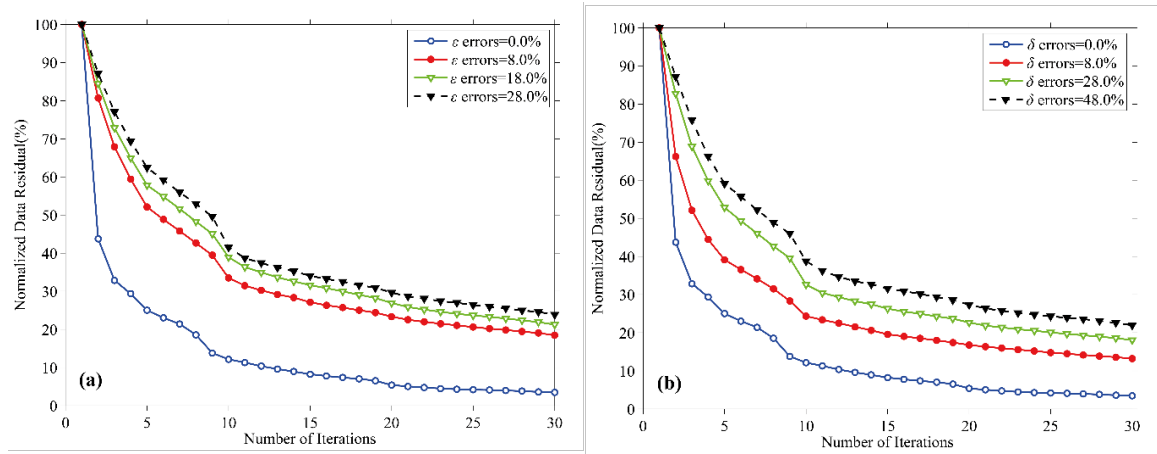


Fig. 16. The curves of the normalized data residual versus the iteration number for LFD-Pre-PLSRTM, when there are errors in (a) ε model and (b) δ model.

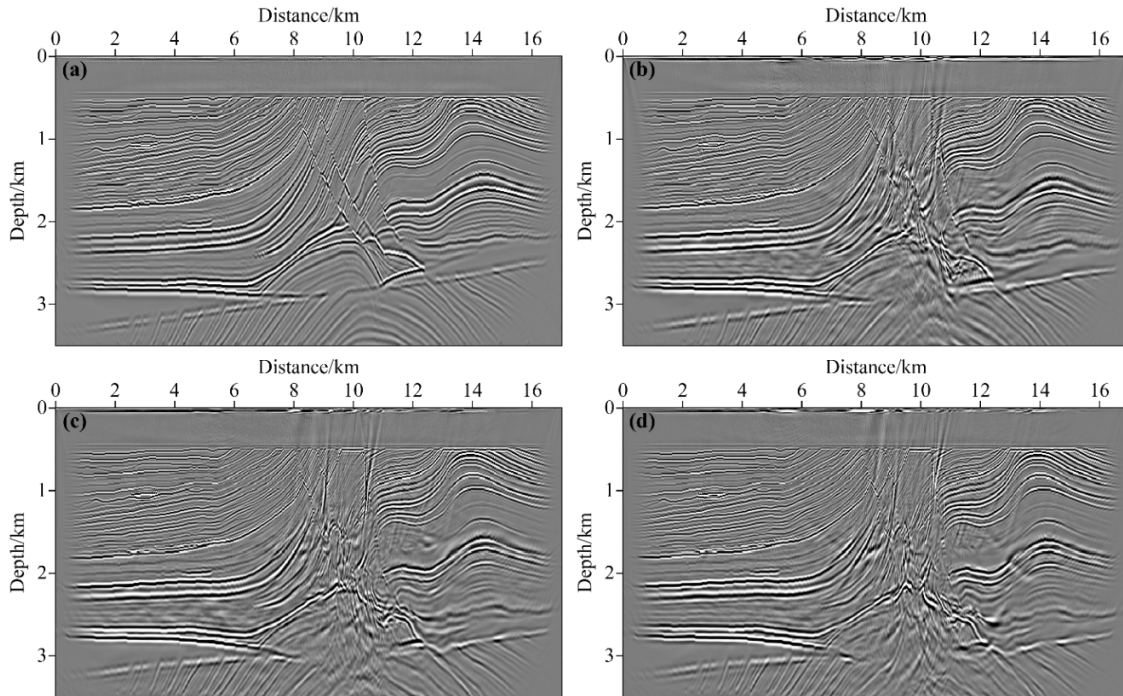


Fig. 17 LFD-Pre-PLSRTM images after 30 iterations by using tilt angle model with a value of (a) 80° (true value), (b) 60° , (c) 30° , and (d) 0° .

CONCLUSION

In this paper, we extend the LFD algorithm from forward modeling to LSRTM, and implement an efficient and stable pure qP-wave LSRTM in anisotropic media. We first derive the pure qP-wave linearized forward modeling and migration operators in TTI media without qSV-wave artefacts. Based on the least-squares migration scheme, we develop LSRTM, which enables us to perform pure qP-wave imaging in TTI media effectively. With the help of the prestack plane-wave technique, both efficiency and

robustness of the proposed method are greatly improved. Finally, two synthetic examples demonstrate the feasibility and applicability of our approach in complex anisotropic media.

(1) The derived pure qP-wave linearized forward modeling and migration operators can not only wholly avoid qSV-wave artefacts, but also provide the accurate source and receiver wavefields, which ensures the effective implementation of LSRTM in anisotropic media;

(2) Compared to PA-LSRTM, the proposed LSRTM based on LFD shows a higher efficiency in the wavefield extrapolation, no limitations on model parameters, and no qSV-wave residuals in the demigration;

(3) The pure qP-wave LSRTM optimized by the prestack plane-wave technique, on the one hand, can significantly reduce the I/O expense and significantly increase the computational efficiency, on the other hand, can effectively improve the robustness of the noise in the data and the errors in the parameter model;

(4) The sensitivity tests of the parameter model error suggest that our method is most sensitive to the velocity model error and the tilt angle model error, moderately susceptible to the ε model error, and insensitive to the δ model error. Therefore, the δ model is the most difficult one to obtain in multi-parameter inversion.

Although the proposed method has shown significant advantages in imaging the pure qP-wave in TTI media, some aspects remain further improved, such as boundary condition and objective function. Therefore, future work will focus on the PML boundary condition based on the low-rank complex matrix decomposition, the inversion process independent on the source wavelet function, and the objective function formulated by the cross-correlation.

ACKNOWLEDGEMENTS

We are grateful to the financial support for this work by China Scholarship Council (CSC), Science and Technology Planning Project of Guizhou Province (QianKeHeJiChu [2020]1Y174), Research Project of Introduced Talent of Guizhou University (GuiDaRenJiHeZi [2018]27), Talent Base Project in Guizhou Province (No. RCJD2018-21), National Oil and Gas Major Project of China (No. 2016ZX05002-005-07HZ, 2016ZX05006-002-003).

REFERENCES

- Alkhalifah, T., 1998. Acoustic approximations for processing in transversely isotropic media. *Geophysics*, 63: 623-631.
- Chen, K. and Sacchi, M.D., 2017. Elastic least-squares reverse time migration via linearized elastic full-waveform inversion with pseudo-Hessian preconditioning. *Geophysics*, 82(5): S341-S358.
- Chu, C., Macy, B.K. and Anno, P.D., 2013. Pure acoustic wave propagation in transversely isotropic media by the pseudospectral method. *Geophys. Prosp.*, 61: 556-567.
- Dai, W. and Schuster, G.T., 2013. Plane-wave least-squares reverse-time migration. *Geophysics*, 78(4): S165-S177.
- Dai, W. and Schuster, J., 2009. Least-squares migration of simultaneous sources data with a deblurring filter. *Expanded Abstr.*, 79th Ann. Internat. SEG Mtg., Houston: 2990-2994.
- Dai, W., Fowler, P. and Schuster, G.T., 2012. Multi-source least-squares reverse time migration. *Geophys. Prosp.*, 60: 681-695.
- Dai, W., Wang, X. and Schuster, G.T., 2011. Least-squares migration of multisource data with a deblurring filter. *Geophysics*, 76(5): R135-R146.
- Dong, S., Cai, J., Guo, M., Suh, S., Zhang, Z., Wang, B. and Li, E.Z., 2012. Least-squares reverse time migration: Towards true amplitude imaging and improving the resolution. *Expanded Abstr.*, 82nd Ann. Internat. SEG Mtg., Las Vegas: 1-5.
- Duan, Y., Guitton, A. and Sava, P., 2017. Elastic least-squares reverse time migration. *Geophysics*, 82(4): S315-S325.
- Dutta, G. and Schuster, G.T., 2014. Attenuation compensation for least-squares reverse time migration using the viscoacoustic-wave equation. *Geophysics*, 79(6): S251-S262.
- Fang, G., Fomel, S., Du, Q. and Hu, J., 2014. Lowrank seismic-wave extrapolation on a staggered grid. *Geophysics*, 79(3): T157-T168.
- Feng, Z. and Schuster, G.T., 2017. Elastic least-squares reverse time migration. *Geophysics*, 82(2): S143-S157.
- Fomel, S., Ying, L. and Song, X., 2010. Seismic wave extrapolation using lowrank symbol approximation. *Expanded Abstr.*, 80th Ann. Internat. SEG Mtg., Denver: 3092-3096.
- Fomel, S., Ying, L. and Song, X., 2013. Seismic wave extrapolation using lowrank symbol approximation. *Geophys. Prosp.*, 61: 526-536.
- Gu, B., Li, Z., Yang, P., Xu, W. and Han, J., 2017. Elastic least-squares reverse-time migration with hybrid l1/l2 misfit function. *Geophysics*, 82(3): S271-S291.
- Guo, P. and McMechan, G.A., 2018. Compensating Q effects in viscoelastic media by adjoint-based least-squares reverse time migration. *Geophysics*, 83(2): S151-S172.
- Hou, J. and Symes, W.W., 2016. Accelerating extended least-squares migration with weighted conjugate gradient iteration. *Geophysics*, 81(4): S165-S179.
- Huang, J., Li, C. and Li, Z., 2017. Plane-wave least-squares reverse time migration in anisotropic media using low-rank finite difference. *Extended Abstr.*, 79th EAGE Conf., Paris..
- Huang, J., Si, D., Li, Z. and Huang, J., 2016. Plane-wave least-squares reverse time migration in complex VTI media. *Expanded Abstr.*, 86th Ann. Internat. SEG Mtg., Dallas: 441-446.
- Liu, Y., Symes, W.W. and Li, Z., 2013. Multisource least-squares extended reverse time migration with preconditioning guided gradient method. *Expanded Abstr.*, 83rd Ann. Internat. SEG Mtg., Houston: 3709-3715.
- Nocedal, J., 1980. Updating quasi-Newton matrices with limited storage. *Mathem. Computat.*, 35(151): 773-782.
- Plessix, R.E., 2006. A review of the adjoint-state method for computing the gradient of a functional with geophysical applications. *Geophys. J. Internat.*, 167: 495-503.
- Qu, Y., Huang, J., Li, Z., Guan, Z. and Li, J., 2017. Attenuation compensation in anisotropic least-squares reverse time migration. *Geophysics*, 82(6): S411-S423.

- Song G., Huang R., Tian J., Chen Y., Chen P., and Yang Y., 2016. A new QP-wave equation for 2D VTI media. Expanded Abstr., 86th Ann. Internat. SEG Mtg., Dallas: 3977-3981.
- Song, X. and Alkhalifah, T., 2013. Modeling of pseudoacoustic P-waves in orthorhombic media with a low-rank approximation. *Geophysics*, 78(4): C33-C40.
- Song, X., Fomel, S. and Ying, L., 2013. Lowrank finite-differences and lowrank Fourier finite-differences for seismic wave extrapolation in the acoustic approximation. *Geophys. J. Internat.*, 193: 960-969.
- Sun, J., Fomel, S., Zhu, T. and Hu, J., 2016. Q-compensated least-squares reverse time migration using low-rank one-step wave extrapolation. *Geophysics*, 81(4): S271-S279.
- Tang, Y., 2009. Target-oriented wave-equation least-squares migration/inversion with phase-encoded Hessian. *Geophysics*, 74(6): WCA95-WCA107.
- Tarantola, A., 1984. Linearized inversion of seismic reflection data. *Geophys. Prosp.*, 32: 998-1015.
- Thomsen, L., 1986. Weak elastic anisotropy. *Geophysics*, 51: 1954-1966.
- Wong, M., Biondi, B. and Ronen, S., 2010. Joint least-squares inversion of up-and down-going signal for ocean bottom data sets. Expanded Abstr., 80th Ann. Internat. SEG Mtg., Denver: 2752-2756.
- Wong, M., Biondi, B.L. and Rone, S., 2015. Imaging with primaries and free-surface multiples by joint least-squares reverse time migration. *Geophysics*, 80(6): S223-S235.
- Wong, M., Ronen, S. and Biondi, B., 2011. Least-squares reverse time migration/inversion for ocean bottom data: A case study. Expanded Abstr., 81st Ann. Internat. SEG Mtg., San Antonio: 2369-2373.
- Xu, S. and Zhou, H., 2014. Accurate simulations of pure quasi-P-waves in complex anisotropic media. *Geophysics*, 79(6): T341-T348.
- Yang, J., Zhu, H., McMechan, G., Zhang, H. and Zhao, Y., 2019. Elastic least-squares reverse-time migration in vertical transverse isotropic media. *Geophysics*, 84(6): S539-S553.
- Zhan, G., Pestana, R.C. and Stoffa, P.L., 2012. Decoupled equations for reverse time migration in tilted transversely isotropic media. *Geophysics*, 77(2): T37-T45.
- Zhan, G., Pestana, R.C. and Stoffa, P.L., 2013. An efficient hybrid pseudospectral/finite-difference scheme for solving the TTI pure P-wave equation. *J. Geophys. Engineer.*, 10(2): 025004.
- Zhang, Y., Duan, L. and Xie, Y., 2015. A stable and practical implementation of least-squares reverse-time migration. *Geophysics*, 80(1): V23-V31.
- Zhang, Y., Zhang, H. and Zhang, G., 2011. A stable TTI reverse time migration and its implementation. *Geophysics*, 76(3): WA3-WA11.